Effects of seed magnetic fields on magnetohydrodynamic implosion structure and dynamics

W. Mostert, V. Wheatley, R. Samtaney, and D. I. Pullin

Citation: Physics of Fluids (1994-present) **26**, 126102 (2014); doi: 10.1063/1.4902432
View online: http://dx.doi.org/10.1063/1.4902432
View Table of Contents: http://scitation.aip.org/content/aip/journal/pof2/26/12?ver=pdfcov
Published by the AIP Publishing

PHYSICS OF FLUIDS **26**, 126102 (2014)

Effects of seed magnetic fields on magnetohydrodynamic implosion structure and dynamics

W. Mostert,[1] V. Wheatley,[1] R. Samtaney,[2] and D. I. Pullin[3]
[1]*School of Mechanical and Mining Engineering, University of Queensland, Queensland 4072, Australia*
[2]*Mechanical Engineering, King Abdullah University of Science and Technology, Thuwal, Saudi Arabia*
[3]*Graduate Aerospace Laboratories, 105-50, California Institute of Technology, Pasadena, California 91125, USA*

(Received 25 July 2014; accepted 12 November 2014; published online 8 December 2014)

The effects of various seed magnetic fields on the dynamics of cylindrical and spherical implosions in ideal magnetohydrodynamics are investigated. Here, we present a fundamental investigation of this problem utilizing cylindrical and spherical Riemann problems under three seed field configurations to initialize the implosions. The resulting flows are simulated numerically, revealing rich flow structures, including multiple families of magnetohydrodynamic shocks and rarefactions that interact non-linearly. We fully characterize these flow structures, examine their axi- and spherisymmetry-breaking behaviour, and provide data on asymmetry evolution for different field strengths and driving pressures for each seed field configuration. We find that out of the configurations investigated, a seed field for which the implosion centre is a saddle point in at least one plane exhibits the least degree of asymmetry during implosion.
 [http://dx.doi.org/10.1063/1.4902432]

I. INTRODUCTION

In Inertial Confinement Fusion (ICF), a small spherical capsule filled with a deuterium-tritium fuel mixture is made to ablate rapidly by very high-energy incident radiation. This causes a shockwave to travel inwards, compressing the fuel to a hot spot of high temperature and pressure to conditions where nuclear fusion can occur.[1]

The effect of adding a seed magnetic field to an ICF implosion with a view to increased performance has been of interest in recent research. Using the OMEGA laser, Knauer *et al.*[2] first investigated laser-driven magnetic field compression, which could amplify a uniform seed field of 50 kG through shockwave compression to tens of megagauss. In further experiments with the OMEGA laser, Hohenberger *et al.*[3] and Chang *et al.*[4] applied a uniform seed field over a target and found increased hot spot ion temperature and neutron yield compared to an unmagnetized target. Perkins *et al.*[5] also numerically examined the effect of a uniform axial seed field on the process, seeing a mitigated effect of shell perturbation amplitude on fusion yield.

In ICF, the material involved becomes rapidly ionized and hence will interact with magnetic fields in a fully coupled manner. Such interactions may be ideally modelled using the equations of magnetohydrodynamics (MHD). Recent computational work has examined case studies of the cylindrical converging MHD Riemann problem under various physically plausible seed field configurations,[6] with room for extension to a detailed parametric study and to the spherical case. Such fundamental studies allow the detailed flow structure that results, which involve multiple families of MHD shocks and rarefactions that may interact non-linearly to be investigated in isolation from confounding physical effects.

Cylindrical implosions with applied seed magnetic fields are of primary interest in the emerging MagLIF concept, outlined by Sefkow *et al.*[7] and references, which uses large axial currents to compress a metallic cylindrical liner through the Lorentz force in a Z-pinch (for a review of the Z-pinch, see Haines[8]), in the presence of a seed axial magnetic field. While differing from ICF in

that it is magnetically driven and features a cylindrical rather than spherical implosion, MagLIF shows increasing promise as an additional technique for producing fusion energy.

Pullin *et al.*[9] have also recently explored the collapse of a cylindrical MHD shock onto a line current of infinite extent, using Whitham's geometrical shock dynamics[10] and computational methods, highlighting some consequences of application of singular seed magnetic fields on the ability of the collapsing shock to compress the target fluid.

Application of a seed field may also affect the behaviour of hydrodynamic (HD) instabilities in converging flows. Awe *et al.*[11] examined three-dimensional instabilities in imploding Z-pinch liners with an applied axial seed field. Hydrodynamic instabilities such as the Richtmyer Meshkov instability (RMI), which occur through the impulsive acceleration, such as by a shockwave, of an interface separating two fluids of different densities,[12] and the Rayleigh-Taylor instability (RTI) also occurs in ICF, acting as a constraint on certain operating parameters.[13] Samtaney[14] showed that growth of the MHD RMI is suppressed under a magnetic field normal to the material interface in certain planar flow configurations and Wheatley *et al.*[15–17] subsequently investigated the mechanism of this suppression. Further research also examined the suppression of the RMI by transverse[18,19] and oblique[20] seed fields for planar MHD flows. Characterizing the dynamics of MHD implosions under the effect of seed fields would assist in a fundamental investigation of the MHD RMI in cylindrical or spherical converging flows, to complement the literature[21–24] on its hydrodynamic counterpart. Figure 1 shows the density field from a preliminary simulation comparing the HD (right) and MHD (left) converging RMI for a uniform, horizontal seed field (see Sec. III), and suggests that the converging MHD RMI is suppressed, but the richness of the flow requires an understanding of the underlying implosion dynamics prior to investigating this type of flow.

This paper characterizes the structure and dynamics of canonical MHD implosions under an applied seed field by examining the converging two-dimensional (cylindrical) and three-dimensional (spherical) MHD Riemann problem, under three different realistic magnetic field configurations. The paper also seeks to quantify the symmetry-breaking effect of the magnetic field on these converging flow features as a function of field strength and driving pressure, since symmetry is a relevant concept in the operation of ICF. In this sense, we seek to provide data that allow for a reasonable assessment of the effect that a particular magnetic field strength and configuration may have on a given implosion.

II. FORMULATION

A. Equations of motion

The variables for ideal MHD are non-dimensionalized as follows:

$$\hat{\mathbf{x}} = \frac{\mathbf{x}}{L_0}, \quad \hat{t} = \frac{t}{L_0/\sqrt{p_0/\rho_0}}, \quad \hat{\rho} = \frac{\rho}{\rho_0}, \quad \hat{p} = \frac{p}{p_0},$$
$$\hat{\mathbf{u}} = \frac{\mathbf{u}}{\sqrt{p_0/\rho_0}}, \quad \hat{\mathbf{B}} = \frac{\mathbf{B}}{\sqrt{\mu_0 p_0}}, \tag{1}$$

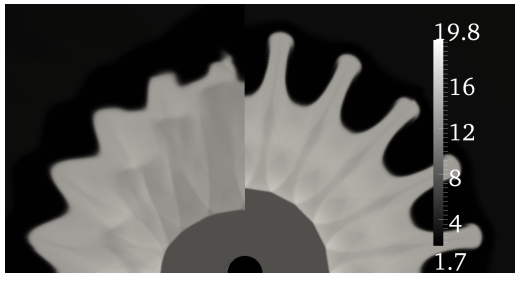

FIG. 1. Density field showing the converging HD RMI (right) and MHD RMI with horizontal seed magnetic field (left), with initial azimuthal perturbation wavenumber of 20, $\beta_{0I} = 2$, Atwood number 0.8 (dense inside) accelerated by a Riemann problem driven shock.

where ρ, $\mathbf{v}$, $\mathbf{B}$, and p are the mass density, velocity, magnetic field, and pressure, respectively, and μ_0 is the permeability of free space.

Under this non-dimensionalization, the equations of ideal magnetohydrodynamics, neglecting the effect of gravity and from here on suppressing the carets for convenience, can be written as[25]

$$\frac{\partial \rho}{\partial t} + \nabla \cdot (\rho \mathbf{v}) = 0, \tag{2}$$

$$\rho\left(\frac{\partial \mathbf{v}}{\partial t} + \mathbf{v} \cdot \nabla \mathbf{v}\right) + \nabla p - (\nabla \times \mathbf{B}) \times \mathbf{B} = 0, \tag{3}$$

$$\frac{\partial p}{\partial t} + \mathbf{v} \cdot \nabla p + \gamma p \nabla \cdot \mathbf{v} = 0, \tag{4}$$

$$\frac{\partial \mathbf{B}}{\partial t} - \nabla \times (\mathbf{v} \times \mathbf{B}) = 0, \quad \nabla \cdot \mathbf{B} = 0, \tag{5}$$

where γ is the ratio of specific heats in the plasma. This model is ideal, neglecting diffusion effects, since they occur over a much larger timescale than advection effects, and considers a continuous quasi-neutral one-fluid plasma. We further model the plasma as a perfect gas, setting $\gamma = 5/3$. The non-dimensional variables are maintained throughout this study.

B. Riemann problem and seed magnetic fields

A Riemann problem describes the flow resulting from the separation of two uniform fluid states by an initial discontinuity. In this investigation, the Riemann problems are set up for three different seed magnetic field configurations, shown in Figure 2, for both cylindrical and spherical geometries. In all cases, the initial condition consists of two uniform quiescent fluids separated by a cylindrical or spherical interface, as appropriate, with a superimposed seed magnetic field. The pressure and density ratios across the interfaces are p/p_0 and ρ/ρ_0, with the reference pressure and density p_0 and ρ_0, respectively, occurring on the inside of the interface, and we represent the effect of the driving pressure with the parameter $\Delta p = p - 1$.

We use Cartesian coordinate systems for both the cylindrical and spherical Riemann problems. The cylindrical geometry (i.e., the cylindrical Riemann problem) is formulated in two dimensions in the (x, y) plane, while the spherical geometry is set in a three-dimensional volume over (x, y, z). The interface is centred at the origin with the reference radius $r_0 = 1$. For convenience, we also define $\phi = \arctan y/x$ with $0 < \phi < \pi/2$ and $\psi = \arctan(z/\sqrt{x^2 + y^2})$ with $0 < \psi < \pi/2$.

Three different seed magnetic fields are tested for each geometry, so that six cases exist in total; cylindrical problems are prefixed with C and spherical with S, with the seed field topology designated by a number 1, 2, or 3. The seed fields are chosen to be physically realizable as potential candidates for use in capsule implosions; for a discussion of how they may be generated physically,

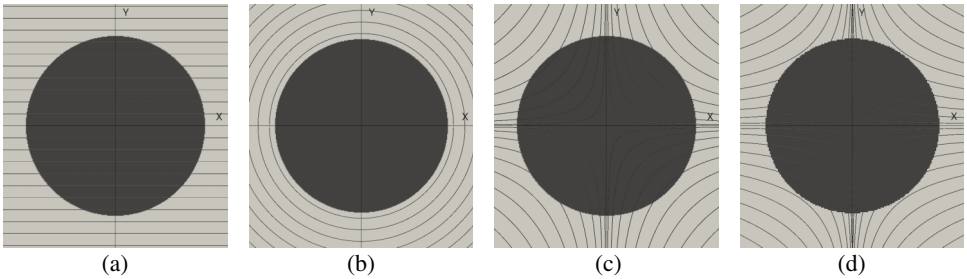

FIG. 2. Pressure fields in the x–y plane with overlaid magnetic field lines showing the initial Riemann interface and field configurations for cases C1-3 and S1-3 in section (at $z = 0$). Higher pressure is lighter-coloured. Field lines in respective C- and S-cases appear identical in the x–y plane, excepting C3 and S3. (a) Case C1, S1 (b) case C2, S2 (c) case C3, and (d) case S3.

see Appendix. The reference seed field strength for any given case is set with the parameter

$$\beta_{0I} = 2\frac{p_0}{B_0^2}, \tag{6}$$

where B_0 is specified for each case below. The subscript I indicates that the parameter is defined according to the reference pressure, and the subscript 0 indicates that it is a reference parameter. An auxiliary parameter is also sometimes used to help describe the reference field strength as a function of the pressure difference across the initial interface

$$\beta_0 = 2\frac{\Delta p}{B_0^2}. \tag{7}$$

The corresponding *local* parameters are $\beta_I = 2p_0/B^2$ and $\beta = 2\Delta p/B^2$, where B is the local field magnitude.

The six cases thus have fields outlined as follows, shown in Figure 2:

C1: Uni-directional field in cylindrical geometry
This is a uniform field, set to the reference strength

$$\mathbf{B} = B_0\hat{\mathbf{e}}_{\mathrm{x}}. \tag{8}$$

C2: Tangential field in cylindrical geometry
Setting $r^2 = x^2 + y^2$ and the tangential unit vector $\hat{\mathbf{e}}_\phi$, this field is zero inside the interface and decays radially outside it according to $1/r$

$$\mathbf{B}(r) = \begin{cases} (B_0 r_0/r)\hat{\mathbf{e}}_\phi & : r \geq r_0 \\ 0 & : r < r_0. \end{cases} \tag{9}$$

Note that the field is discontinuous at $r = r_0$.

C3: Saddle field in cylindrical geometry
This field present a saddle configuration in the domain and is defined by

$$\mathbf{B}(x,y) = \sum_{i=1}^{4}\left\{\frac{\alpha_i B_0}{(x-x_i)^2 + (y-y_i)^2}\right. \\ \left.\left[-(y-y_i)\hat{\mathbf{e}}_{\mathbf{x}} + (x-x_i)\hat{\mathbf{e}}_{\mathbf{y}}\right]\right\}, \tag{10}$$

where $\alpha_i = \{+\alpha_0, -\alpha_0, -\alpha_0, +\alpha_0\}$ is a signed scaling parameter that sets $|B(r_0)| = B_0$; and $(x_i, y_i) = \{(10,10),(-10,10),(-10,-10),(10,-10)\}$.

S1: Uni-directional field in spherical geometry
A uniform field, as in C1

$$\mathbf{B} = B_0\hat{\mathbf{e}}_{\mathbf{x}}. \tag{11}$$

S2: Tangential field in spherical geometry
This field is a three-dimensional analogue of C2. Setting $r^2 = x^2 + y^2 + z^2$ and $\eta^2 = x^2 + y^2$,

$$\mathbf{B}(r,\eta) = \begin{cases} (B_0 r_0/\eta)\hat{\mathbf{e}}_\phi & : r > r_0, \eta \geq r_w \\ (B_0 r_0 \eta/\eta_w^2)\hat{\mathbf{e}}_\phi & : r > r_0, \eta < r_w \\ 0 & : r < r_0, \end{cases} \tag{12}$$

where η_w is a parameter that sets an "arc width" along the z-axis outside the interface and $r_0/\eta_w = 15$. In this way, the magnetic field remains planar in x–y. The field is discontinuous at $r = r_0$ and in its η-derivative at η_w for $r > r_0$.

S3: Saddle field in spherical geometry
This field is a three-dimensional analogue of C3, and is given by

$$\mathbf{B}(x,y,z) = B_x\hat{\mathbf{e}}_{\mathbf{x}} + B_r\hat{\mathbf{e}}_{\mathbf{r}}, \tag{13}$$

with $r^2 = y^2 + z^2$ and $\hat{\mathbf{e}}_\mathrm{r}$ is the radial unit vector in the y–z plane. This field results from setting two opposite current loops in the y–z plane, centred on the x-axis at $x_i = \{7, -7\}$, and the field components are derived from Smythe[26] to give

$$B_x = \sum_{i=1}^{2} \alpha_i B_0 \frac{1}{\pi\sqrt{Q_i}} \left[E(k_i) \frac{1 - \varrho^2 - \chi_i^2}{Q - 4\varrho} + K(k_i) \right], \tag{14}$$

$$B_r = \sum_{i=1}^{2} \alpha_i B_0 \frac{\xi_i}{\pi\sqrt{Q_i}} \left[E(k_i) \frac{1 + \varrho^2 + \chi_i^2}{Q - 4\varrho} - K(k_i) \right], \tag{15}$$

where $a = 7$ is a "current loop radius," set to be consistent with Chang *et al.*;[4] $Q_i = (1 + \varrho)^2 + \chi_i^2$, $k = \sqrt{\frac{4\varrho}{Q_i}}$, $\varrho = r/a$, $\chi_i = (x - x_i)/a$, and $\xi_i = (x - x_i)/r$. K and E are elliptic integrals of the first and second kind, respectively.

C. Parameter space

To determine the effect of driving pressure and magnetic field strength on the symmetry of the converging flow, we investigate the six cases, for various driving pressures $\Delta p = p - 1$ and β_{0I}. As we will note later in this paper, there is a critical $\beta_{cI} = 2/\gamma$ for which the character of the implosion changes. We define $\beta_{0I} > \beta_{cI}$ as *subcritical* and $\beta_{0I} < \beta_{cI}$ as *supercritical* field strengths. The cases C1-3 we test under the following values, including both subcritical and supercritical magnetic field strengths:

$$\Delta p = 2, 4, 8, 16, 25,$$

$$\beta_{0I} = 128, 32, 8, 2, \frac{1}{2}, \frac{1}{8}, \frac{1}{32}, \frac{1}{128}.$$

Along a field angle of $\theta = 0$, these Δp provide an initial sonic Mach number of

$$M \simeq 1.24, 1.43, 1.75, 2.24, 2.68,$$

respectively, for the hydrodynamic shocks at that angle. Away from this angle, the shock types change, and the characteristic speed used to calculate magnetosonic Mach numbers will vary with both θ and β_{0I}. The shocks also accelerate as they converge. These Mach numbers are therefore a guide only, valid only for the very early stage of the flow, along $\theta = 0$.

For cases S1-3, we investigate the following Δp and β_{0I}, the latter of which all are subcritical:

$$\Delta p = 2, 4, 8,$$

$$\beta_{0I} = 128, 32, 8, 2.$$

Note that in existing literature such as Hohenberger *et al.*[3] and Chang *et al.*,[4] the seed fields and pressure capsules are such that under our definition of field strength, β_{0I} is very small; however, taking into account the large Δp, the parameter β_0 is very large. Given the fundamental nature of this study, we use β_{0I} since the effect of a seed field on flow symmetry proves to be more easily characterized if the effect of the driving pressure jump Δp is not embedded in the strength parameter (see Sec. IV B 1). In any case, the range of Δp considered here does not extend to the large driving pressures seen in ICF experiments.

III. METHODOLOGY

A. Numerical method

We solve the flows numerically using a second-order accurate, non-linear compressible finite volume code developed by Samtaney[27] for solving the ideal MHD equations, using a dimensionally unsplit upwinding method with a Roe-type flux solver. A projection method is used to enforce the solenoidal property of the magnetic field.

The grid for cases C1 and C3 is a uniform cartesian 800^2 mesh discretizing $-l < x, y < l$, where $l = 10/3$; the grid for C2 is mapped to cylindrical co-ordinates for a 1024^2 mesh, discretizing $l/20 < r < 5l/6$ and $0 < \phi < 2\pi$. The same grid is used for the RMI simulation whose results are shown in Figure 1, discretizing $l/25 < r < 2l/3$ and $0 < \phi < \pi$.

For cases S1-3, we additionally use adaptive mesh refinement of the Berger-Collela type[28] under the Chombo framework,[29] on a Cartesian mesh (including S2). We simulate on the full domain, discretizing $-l < x, y, z < l$, on a Cartesian 64^3 mesh with three levels of refinement, with a refinement ratio of 2 in each direction. The criterion for refinement is $|\nabla\rho| > 0.02\rho$ on the local ρ. This yields an effective resolution of 512^3 at features in the flow where density jumps occur.

B. Characterisation and parameters

We characterize each case by identifying the types and behaviours of waves appearing in each solution. The chosen driving pressure and initial magnetic field strength for characterisation are taken as $\Delta p = 2$, $\beta_{0I} = 2$ in order to provide a flow with comparable thermodynamic and magnetic effects. First, we designate θ as the local angle between the magnetic field and the wave propagation direction, and assume that at early times, the waves generated by the cylindrical and spherical Riemann problems match those in the equivalent one-dimensional (1D) Riemann problems with equivalent θ. Next, we explain features that form in the developed flow of the cylindrical and spherical problems which do not appear in the 1D equivalents by examining local pressure and density fields. The mode of convergence is then examined, since the presence of a magnetic field affects the symmetry of the converging flow.

To study the effect of magnetic field and driving pressure on the symmetry of the converging flow, we vary β_{0I} and Δp. For measuring the effect of magnetic field on symmetry of the converging flow in cases 1 and 3, we define the major and minor axes for the primary shock system and the material interface formed by the Riemann problem, where the primary shock system is identified as the shock system with the strongest effect on pressure as it converges. Since C2 remains axisymmetric throughout its evolution (see Sec. IV), it is not examined, though we do consider S2. We conclude by conducting a parametric study of the implosion symmetry as a function of time, magnetic field strength, and interface pressure ratio.

We define a major axis as *the axis along which the primary shock system is initially travelling most slowly*, and similarly the minor axis as *the axis along with the primary shock system is initially travelling most quickly*. The symmetry parameter σ of the primary shock system and the material interface is defined as the ratio of the minor to major axes of the discontinuity in question.

For the symmetry studies, particularly the cylindrical cases, there is a change in character of the waves in the implosion; here, we derive the critical parameter that governs, in part, this change in character. The fast and slow characteristic speeds in ideal MHD are given by[25]

$$c_{f,s}^2 = \frac{1}{2}\left(\frac{\gamma p + \mathbf{B}\cdot\mathbf{B}}{\rho} \pm \sqrt{\left(\frac{\gamma p + \mathbf{B}\cdot\mathbf{B}}{\rho}\right)^2 - 4\frac{\gamma p B_n^2}{\rho^2}}\right), \tag{16}$$

where subscripts f and s refer to the fast and slow speeds, respectively. The magnetic field component B_n here is the component parallel to the wave propagation, so that $B_n = B\cos\theta$. Using the Alfvén speed $c_A = \sqrt{B^2/\rho}$, the intermediate speed $c_I = \sqrt{B_n^2/\rho}$, and the gas-dynamic sound speed $c = \sqrt{\gamma p/\rho}$, we write

$$c_{f,s}^2 = \frac{1}{2}\left((c_A^2 + c^2) \pm \sqrt{(c_A^2 + c^2)^2 - 4c_I^2 c^2}\right). \tag{17}$$

Taking the square-root term as necessarily positive, we note that for the special case $\theta = 0$,

$$c_{f,s}^2 = \frac{1}{2}\left(c_A^2 + c^2 \pm |c_A^2 - c^2|\right) \tag{18}$$

and that this special case provides a minimum for c_f and a maximum for c_s. Furthermore, for $c_A < c$, the fast speed c_f is degenerate with the sonic speed c and the slow speed c_s is degenerate

with the Alfvén c_A, and for $c_A > c$, the reverse is true. Recognizing this change in character, and that $\beta_{0I} = 2c^2/(\gamma c_A^2)$, we define the critical field strength parameter

$$\beta_{cI} = \frac{2}{\gamma}, \tag{19}$$

which is defined at $\theta = 0$. Therefore, we refer to a $\theta = 0$ field along where $\beta_I < \beta_{cI}$ as *supercritical*, since for these fields $c_A > c$, and a $\theta = 0$ field where $\beta_I > \beta_{cI}$ is *subcritical*, since here $c_A < c$.

Although we define β_{cI} only at $\theta = 0$, hence making it only an essentially local parameter, it proves to have a significant effect on the global character of the flow. For this reason, and for convenience, we will globally refer to a given flow as supercritical or subcritical according to the initial β_I/β_{cI} at $\theta = 0$, on the Riemann interface.

It is possible that, for flows where the field strength is not much greater than the critical, a shock system may compress a $\theta = 0$ flow region from supercritical to subcritical conditions, so that the speed degeneracy in that region is ambiguous. We will refer to flows such as these as *transcritical*.

Criticality is not relevant to case 2 problems since, in all formulations, the field is nowhere initially normal to the Riemann interface, and hence β_{cI} is not defined.

C. Numerical convergence

The grid used for the cylindrical cases was tested for convergence with a uniform mesh which is described in Sec. III, using Richardson extrapolation under monotonic convergence as described by Stern *et al.*[30] The full evolution of the symmetry parameter σ is shown for case C1 in Figure 3(a) for the uniform meshes of 450^2, 600^2, and 800^2. Both the primary shock and material interface symmetry data converge monotonically for most times. To define order of convergence, we use a representative value of σ at 75% convergence time, σ_{75}. The σ_{75} for the primary shock system is interpolated for each mesh, and found to converge with order $\simeq$1.69, with an estimated relative error on the finest mesh of 0.41%.

For the adaptive mesh used for spherical cases, convergence was examined similarly with three base (unrefined) resolutions set to 36^3, 48^3, and 64^3, corresponding, with three levels of adaptive refinement to effective resolutions of 288^3, 384^3, and 512^3, respectively. The σ evolution of this case (S1) is shown in Figure 3(b), with the primary shock data time-averaged for each curve on a 3-point window to filter numerical oscillation associated with the calculation of σ (see Subsection IV B). The time-averaged primary shock data converge monotonically, while the material interface data converge such that the medium- and fine-mesh curves are nearly indistinguishable, with oscillatory noise in the time histories dominating the difference between them, rather than a consistent error due to varying grid resolution. The σ_{75} is determined from the interpolated, time-averaged primary shock data and found to converge with a calculated order of $\simeq$2.47. Since the numerical method in use is a second-order method, this convergence order is limited to 2, with an associated estimated relative error of 0.97% on the finest mesh.

IV. RESULTS

A. Characterisation of cylindrical cases

The developed flows for cases C1-3 under $\Delta p = 2$, $\beta_{0I} = 2$ are shown in Figure 4. Pressure is used in order to visualize the MHD shocks and tangential discontinuities and their approximate strengths, although it does not show MHD contact discontinuities. Cases C1 and C3 are clearly non-axisymmetric, while C2 is axisymmetric.

By configuration, case C1 shows $\theta \simeq \phi$; C2 shows a constant $\theta = \pi/2$; and C3 shows $\theta \simeq \phi/2$. Figure 4 reflects that there is a θ-ϕ dependence for the respective cases; the axisymmetric θ in case 2 corresponds with the axisymmetric wave behaviour, for example.

For each case, at early times, the waves along a given ϕ-ray match those generated from a one-dimensional Riemann problem with equivalent θ. Visible in Figure 4, they appear in the flows as follows, from the domain centre outwards:

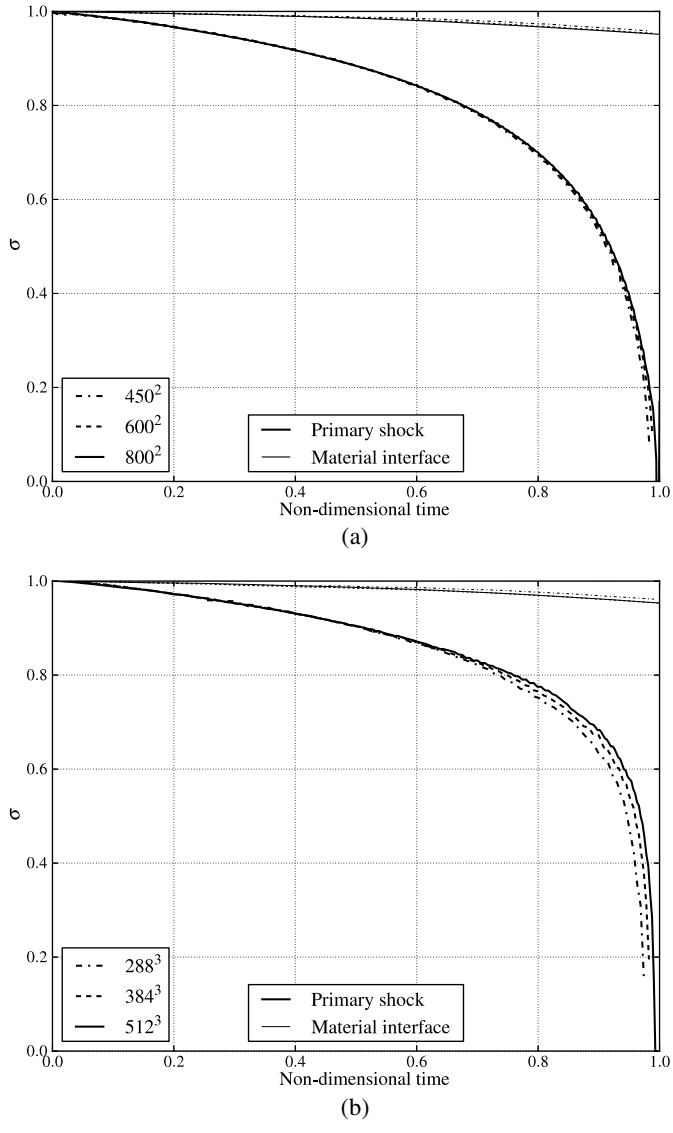

FIG. 3. Symmetry parameter evolution for C1 and S1, showing material interface and primary shock symmetry. S1 primary shock σ data smoothed with a 3-point moving average. (a) Case C1, uniform mesh and (b) case S1, adaptively refined mesh.

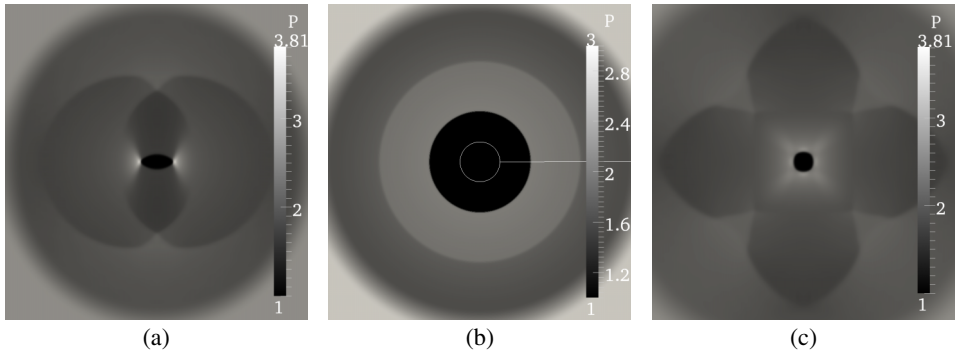

FIG. 4. Developed pressure fields for cases C1-3, $\beta_{0I} = 2$, $\Delta p = 2$. Mesh boundaries shown in white outline for C2. (a) Case C1, $t = 0.46$, (b) case C2, $t = 0.33$, and (c) case C3, $t = 0.51$.

- Cases C1 and C3—a fast MHD shock system; a slow MHD shock system; the material interface (not visible in Figure 4); a slow MHD expansion wave system; and a fast MHD expansion wave system. These systems are non-axisymmetric.
- Case C2—an HD shock system; the material interface; a fast MHD expansion wave system. These systems are axisymmetric.

The material interface is characterized as an MHD contact discontinuity (CD) for $\theta \neq \pi/2$, which is discontinuous only in density, and as an MHD tangential discontinuity (TD) for $\theta = \pi/2$, which allows for discontinuity in density, pressure, and (tangential) magnetic field but requires continuous total pressure $p_{tot} = p + B^2/2$ and occurs where there is no normal magnetic field component. The C2 material interface is thus everywhere a TD. The TD also supports the magnetic field discontinuity that initially exists at $r = r_0$, maintaining the field to be zero inside. As Figure 4 shows, the slow MHD shock and wave systems are not defined at $\theta = 0$ in the reference case. This is because of the speed degeneracies at $\theta = 0$, where the flow is essentially HD and is common to subcritical problems; for supercritical problems, the fast MHD systems become undefined at $\theta = 0$ (see Subsections IV B 1 and IV B 2).

In intermediate times, singularities in the shock structure (kinks) can be seen in cases C1 and C3. These develop due to a dependence of the shock speed on θ and the continuous acceleration of the converging waves. In Figure 4, they are visible in C1 along $\phi = \pm\pi/2$ in the slow shocks and $0, \pi$ in the fast shocks; in case C3, along $\phi = \pm\pi/4, \pm 3\pi/4$ (slow shocks) and $0, \pm\pi/2, \pi$ (fast shocks). The kinks generally resemble regular reflection behaviour in HD shocks.

To examine kink structure, Figure 5 shows the $\phi = \pi/2$ slow shock kink in case C1 at time $t = 0.57$, having first appeared at around $t \simeq 0.27$. The overlaid streamlines are the flow velocity in a reference frame in which the kink is stationary. Though the material interface at $\phi = \pi/2$ was initially a TD, the formation of this kink from the surrounding slow shock structure has decomposed the TD into a CD and a slow shock. Vorticity is used to show the wave positions, while density shows the location of the contact surface, which is clearly separated from the slow shocks close to the kink.

The slow shock system near the kink causes the flow to converge horizontally; additional reflected shocks to form to straighten the flow and maintain continuity. These reflected shocks extend to the nearby contact surface where they connect with the slow expansions further out.

In all simulations, kinks in shocks appear at local minima in their corresponding magnetosonic speeds. In cases C1 and C3, minima in slow magnetosonic speeds occur at $\theta = \pi/2$, and in fast magnetosonic speeds at $\theta = 0$. Case C2 shows no kinks because θ remains constant for all ϕ.

Convergence occurs when the primary shock system reaches the centre of the domain. Cases C1 and C3 show a non-axisymmetric convergence event; Figure 6 shows the pressure distribution around the domain centre around convergence time for these cases under the same colour scale.

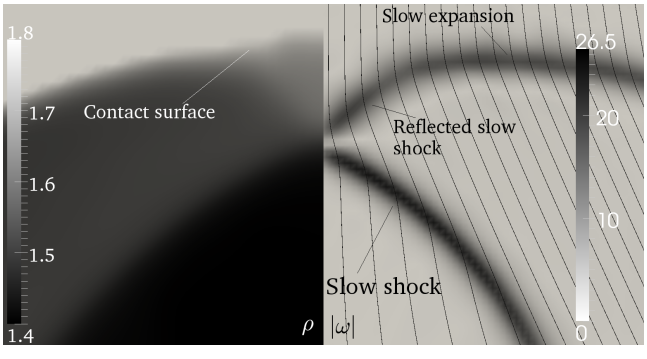

FIG. 5. Closeup view of kink in case C1 converging slow shock along $\phi = \pi/2$, $t = 0.43$, showing density (left) and vorticity magnitude (right). Velocity streamlines, in a reference frame in which the kink is stationary, are superimposed on the vorticity graph, and indicated an upward flow.

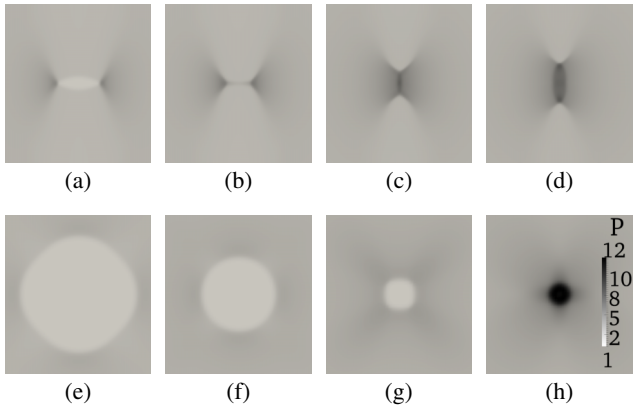

FIG. 6. Case C1 (a)-(d) and C3 (e)-(h) pressure fields at domain centre near convergence, $\beta_{0I} = 2$, $\Delta p = 2$. Note higher pressure is darker coloured. (a) $t = 0.483$, (b) $t = 0.500$, (c) $t = 0.533$, (d) $t = 0.550$, (e) $t = 0.463$, (f) $t = 0.500$, (g) $t = 0.533$, and (h) $t = 0.567$.

In both cases, the $\theta = \pi/2$-fast shocks move more quickly than the kink-carrying $\theta = 0$-fast shocks. In case C1, this means that the $\theta = \pi/2$-shocks converge at a distinctly earlier time than the $\theta = 0$-shocks; by the time that the $\theta = 0$-shocks converge, the $\theta = \pi/2$-shocks have already reflected off each other at the centre. However, the convergence event for case C3 is much more a distinct, single event, due to an increased symmetry in the fast shock structure near convergence time. The reasons for these differences in symmetry are discussed further below.

For case C2, convergence qualitatively resembles an HD convergence, since it is axisymmetric and the converging shock structure is HD.

B. Symmetry of cylindrical cases

We now examine the effect of the seed field on the symmetry of cases C1 and C3. Since it remains axisymmetric, we omit C2. The symmetry parameter σ is defined as the ratio of the minor to the major axes, with these axes defined in Sec. III. We present figures showing the evolution of σ over time for a given parameter choice, where the time has been normalized to the time of convergence (that is, when the primary shock system first reaches the domain centre). For brevity, we present these symmetry evolution curves for selected parameters, usually for $\beta_{0I} = 2$, $\Delta p = 2$, to show the pertinent effects in their most obvious forms. Pressure contour maps are also included to show visually the various degrees of effect from the seed field. We also use a single value to represent the effect of the field, to allow easy comparison across the parameter space. For flows where σ varies monotonically over time, we represent the "flow symmetry" with σ at 75% of the convergence time, σ_{75}. For non-monotonic symmetry evolution curves, we select the minimum value σ_{min} on the graph. The symmetry evolution curves throughout the results are smoothed with a moving-average scheme to reduce oscillations. These oscillations arise from the numerical discretisation of the domain and that σ is derived from a quotient of two shock positions.

1. Case C1

Beginning with the reference case parameters, $\Delta p = 2$, $\beta_{0I} = 2$, Figure 7 shows the evolution of the symmetry parameter σ as the flow converges for the primary shock system—in this case, the fast shock system, as characterized above—and the contact surface. The decrease is monotonic for both jumps. The primary shock system approaches a σ of zero, since by definition at convergence the minor axis (in this case at $\phi = \pi/2$ in the flow) reaches zero length. In contrast, the contact surface maintains a much higher degree of symmetry—in fact, the decrease in σ for the contact surface is due to the relative "bulge" at $\pi/2$, which is visible in the density field in Figure 5. This case is subcritical.

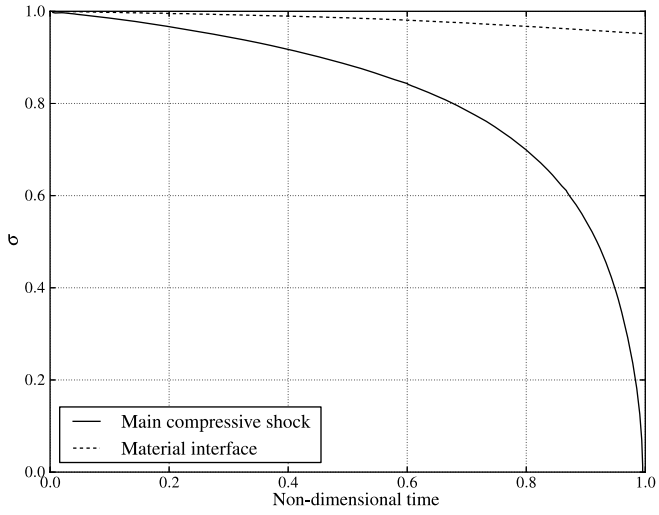

FIG. 7. Evolution of the symmetry parameter for the fast shock system and material interface in case C1, with $\beta_{0I} = 2$, $\Delta p = 2$, normalized to convergence time. Both curves have been smoothed with a 3-point moving average.

Looking across the parameter space now, the development of asymmetry in subcritical cases across β_{0I} can be seen in Figure 8. Strongly subcritical cases (that is, $\beta_{0I} \gg \beta_{cI}$) appear nearly degenerate with the HD converging Riemann problem. The fast shock system, which is the primary shock system in all subcritical cases, resembles the corresponding HD shock system, while the slow shock system is not easily visible. Increasing the field strength up to $\beta_{0I} = 2$, the fast shock system becomes weaker in terms of pressure jump and the slow shock system becomes strong, until we eventually reproduce the reference case characterized above. The faint patterning inside the outer expansions consists of very weak secondary waves resulting from our use of an unregularized Riemann interface. These waves do not appear to influence the large-scale behaviour of the flows.

For $\beta \ll \beta_c$ (supercritical field), the fast shocks have weakened to very low strength, and the slow shock system has become the primary shock system. Here, the HD shock at $\phi = 0$ is a slow shock. Figure 9 shows how the (slow) shock geometry is much more insensitive to variation in both β and Δp.

Figure 10, which sets $\beta_{0I} = 1/2$, shows that, for fields near the critical value, there is less clear separation between the fast and slow shocks in the vicinity of $\phi = 0$. Though this field is by strict definition supercritical, the fast shocks are not very weak. For low $\Delta p(=2,4)$, the field is supercritical both upstream and downstream of the fast shock system, so that the HD shock is connected to the slow shock system, and the $\phi = 0$ discontinuity in the fast system is a fast-shock kink. For high $\Delta p(>16)$, the fast shock system is strong enough to make its downstream field locally subcritical (since the local pressure has increased such that $|B| < \sqrt{\gamma p}$), so that the slow shocks do not degenerate to an

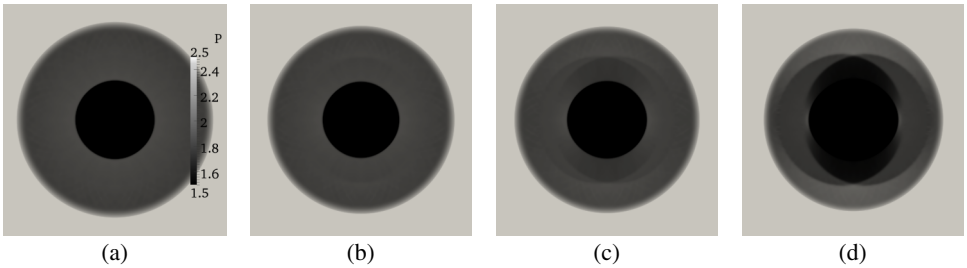

FIG. 8. Pressure field (consistent scale), showing the appearance of asymmetry in case C1 with increasing magnetic field strength. $\Delta p = 2$ in all simulations. (a) $\beta_{0I} = 128$, $t = 0.29$, (b) $\beta_{0I} = 32$, $t = 0.29$, (c) $\beta_{0I} = 8$, $t = 0.27$, and (d) $\beta_{0I} = 2$, $t = 0.2$.

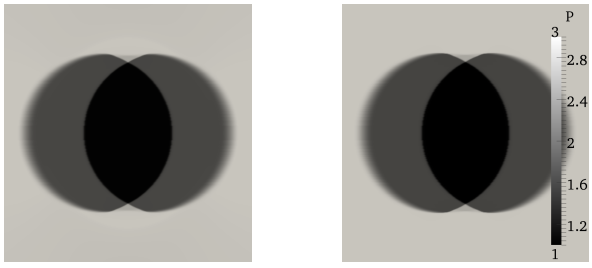

(a) (b)

FIG. 9. Comparison of pressure field between two supercritical C1 flows. $\Delta p = 2$ for both flows. Only the slow shock and expansion systems are visible, the fast shocks having weakened at these β. (a) $\beta_{0I} = 1/32$, $t = 0.28$ and (b) $\beta_{0I} = 1/128$, $t = 0.28$.

HD shock at $\phi = 0$. For these high driving pressures, an HD Mach stem forms that joins the fast and slow shock systems through Mach reflection, as seen around $\phi = 0$ in Figure 10(c).

The fast shocks become weaker with increasingly supercritical β_{0I}. As pointed out in Sec. III, the $\theta = 0$ fast characteristic speed is degenerate with the Alfvén speed and for this reason the fast shocks in the vicinity of $\theta = 0$ cannot degenerate to an HD shock. Furthermore, for small θ, the fast shocks are necessarily weak: we recognize that for $c_A \gg c$,

$$c_f \simeq c_A, \tag{20}$$

so

$$\frac{c_f}{c_I} \simeq \frac{c_A}{c_I} = \frac{1}{\cos\theta}, \tag{21}$$

which remains small (<1.1) for $\theta < \pi/8$. Since, for these angles, the fast magnetosonic speed is only slightly higher than the intermediate speed, therefore the velocity jump across a corresponding fast shock must be small for the shock to remain fast-mode. The allowable velocity jump across the shock increases with θ; however, the shock remains quite weak for these higher ϕ to maintain continuity along with its (necessary) weakness at low ϕ.

The slow shocks are not constrained in the same way, since for $c_A \gg c$,

$$c_s^2 \simeq \frac{c_I^2 \cos^2\theta}{2}\left(1 - \sqrt{1 - \frac{4c^2\cos^2\theta}{c_A^2}}\right), \tag{22}$$

which reduces to

$$\frac{c_s}{c_I} \simeq 0, \tag{23}$$

or equivalently,

$$c_I \gg c_s, \tag{24}$$

which allows for large velocity jumps across slow shocks, regardless of θ.

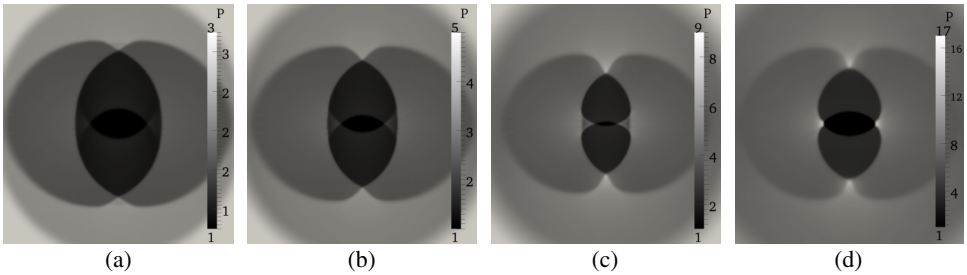

(a) (b) (c) (d)

FIG. 10. Comparison of pressure field between transcritical ($\beta_{0I} = 1/2$) C1 flows. (a) $\Delta p = 2$, $t = 0.31$, (b) $\Delta p = 4$, $t = 0.31$, (c) $\Delta p = 8$, $t = 0.30$, and (d) $\Delta p = 16$, $t = 0.23$.

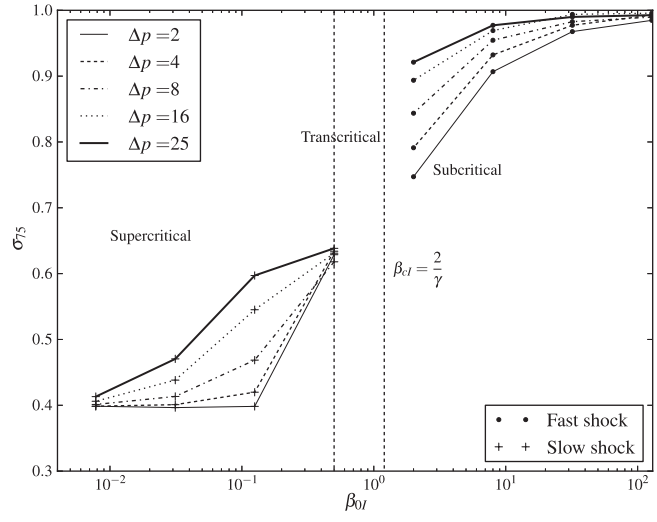

(a)

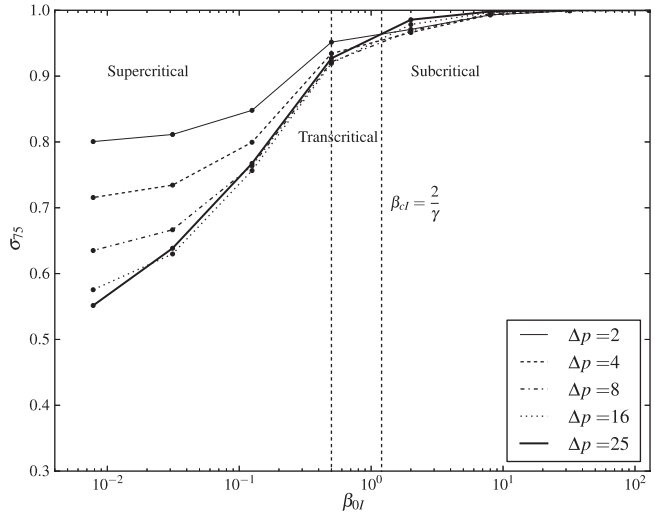

(b)

FIG. 11. Symmetry of the (a) primary shock system and (b) material interface for varying β_{0I} and Δp, measured at 75% the convergence time in case C1. Note that the primary shocks are fast for $\beta_{0I} > \beta_{cI}$ and slow for $\beta_{0I} < \beta_{cI}$. Vertical dashed line indicates β_{cI}.

Although the fast shocks are quite weak for supercritical fields in C1, they do still strengthen as they converge. Consequently, on convergence and reflection of the domain centre, they propagate outwards and may interact with the still-imploding slow shock system. Since these reflected fast shocks are strongest at $\theta = \phi = \pi/2$, they would most strongly affect the slow shock system at that angle, and thus slightly affect the symmetry parameter evolution. This effect occurs most obviously for $\beta_{0I} = 1/8$.

Corresponding with the decrease in fast shock strength, the slow shocks must get stronger with decreasing β_{0I}, since the total pressure jump Δp must be accounted for. The insensitivity of the slow shock geometry to supercritical β_{0I} corresponds with the insensitivity to the bounds of c_s to β_{0I}.

The effect of increasing Δp primarily reduces the time of convergence and increases the pressure jumps across the shocks. It also positively affects the symmetry of the primary shock system, whether fast or slow.

Figure 11 shows the variation of primary shock and contact surface symmetry over the parameter space. It shows a general decrease in σ_{75} with β_{0I}, as discussed above. Note that the decrease

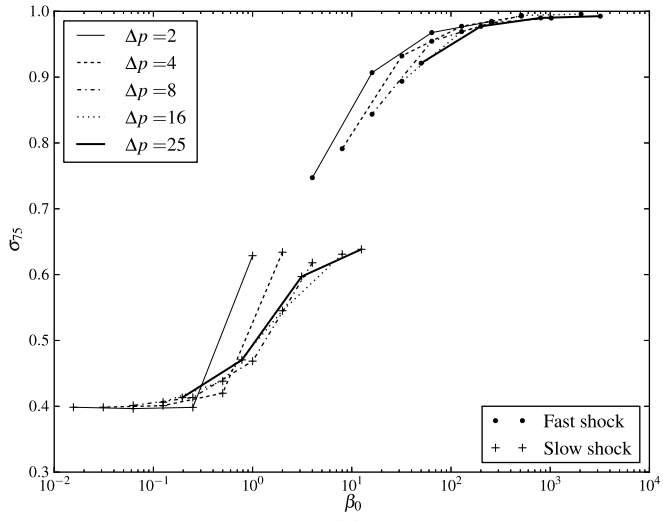

(a)

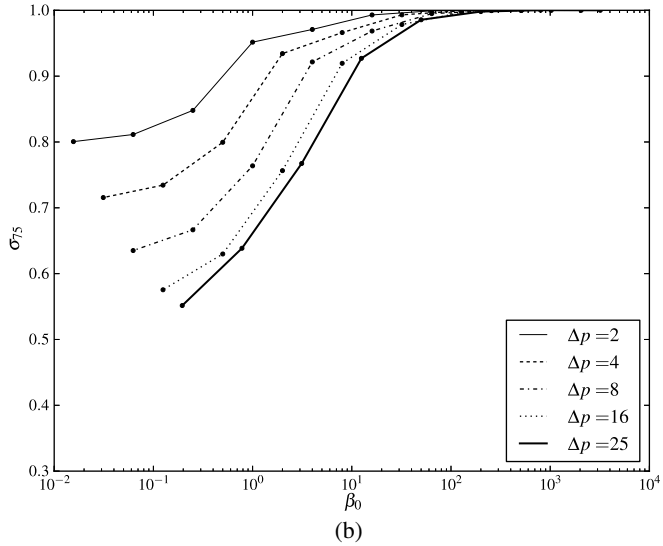

(b)

FIG. 12. Symmetry of the (a) primary shock system and (b) material interface plotted over $\beta_0 = 2\Delta p / B_0^2$, measured at 75% convergence time in case C1.

in symmetry occurs for both fast (for subcritical flows) and slow (for supercritical) primary shock systems. As discussed above, an increase in Δp corresponds with an increase in σ_{75} across the parameter space and so remains sensitive to both β_{0I} and Δp. On the other hand, strongly supercritical fields, due to the invariance of slow shock geometry with β_{0I}, show reduced variation in σ_{75}. The contact surface is however only lightly sensitive to β_{0I} and Δp for subcritical fields, though for supercritical fields, it becomes more sensitive.

This increased sensitivity of the contact surface on field and pressure for strongly supercritical β_{0I} is probably due to the continuing strengthening of the slow shock system, which, around the $\theta = \pi/2$ kink, may cause a sharper discontinuity in the contact surface geometry, causing it to "bulge" more strongly. This would also explain the symmetry reducing effect of increasing Δp. For subcritical fields, where the slow shock system geometry is not yet fully developed and still quite weak, an increased Δp does not translate as immediately into a stronger discontinuity in contact surface geometry.

Plotting the symmetry data over the alternative field strength parameter, $\beta_0 = 2\Delta p / B_0^2$, as in Figure 12, appears to show a general increase of the symmetry parameter with β_0, although the data

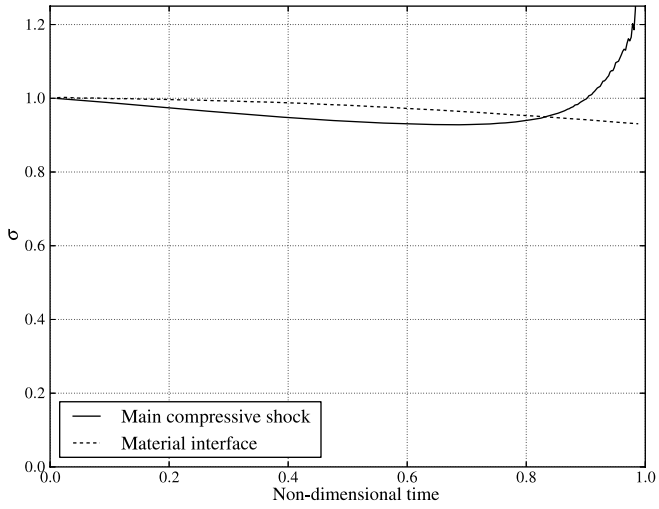

FIG. 13. Evolution of the symmetry parameter for the fast shock system and material interface in case C3, with $\beta_{0I} = 2$, $\Delta p = 2$, normalized to convergence time. Both curves have been smoothed with an 11-point moving average.

do not universally collapse. However, presenting the data over β_{0I} most clearly highlights where the change in character of the converging waves and hence the symmetry of the problem occurs. β_{0I} is better suited for this presentation since it more faithfully represents the upstream conditions for the initially generated waves in the Riemann problem. Under this presentation, Δp has a secondary influence on the symmetry parameter (which we continue to observe in the results below, except for transcritical C1 flows).

2. Case C3

Figure 13 shows the evolution of σ over time for the reference case, $\beta_{0I} = 2$, $\Delta p = 2$, under the C3 field configuration. In contrast to the C1 evolution curve, this curve is not monotonic, exhibiting a turning point as the shocks approach convergence. As the shocks approach the centre, the magnetic field strength decreases approximately linearly to zero; for supercritical β_{0I}, this allows a transition to subcritical upstream conditions for the primary shock system along $\theta = 0$; furthermore, for all β_{0I}, c_A approaches zero towards the centre, so that c_f for $\theta \neq 0$ approaches c, i.e., the shocks become HD for all θ, and the shock system approaches uniform convergence rates across ϕ, kinks aside. This explains why the σ evolution curve has a turning point.

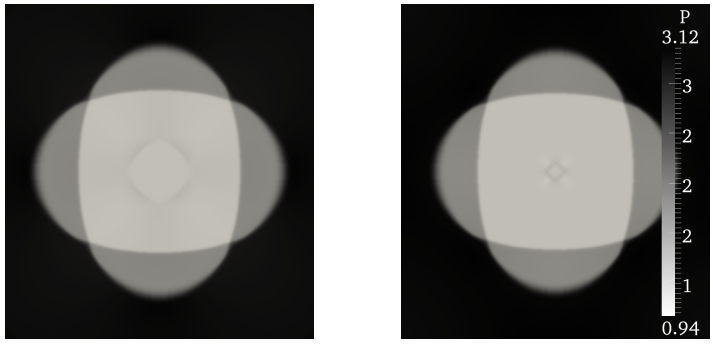

(a) (b)

FIG. 14. Pressure fields under C3 at the same time $t = 0.15$ for (a) $\beta_{0I} = 1/32$ and (b) $\beta_{0I} = 1/128$ and initial pressure jump $\Delta p = 2$ showing insensitivity of the slow shock structure to magnetic field strength, and the fast shock structure near the domain centre. Higher pressure is darker coloured to show the fast shock systems.

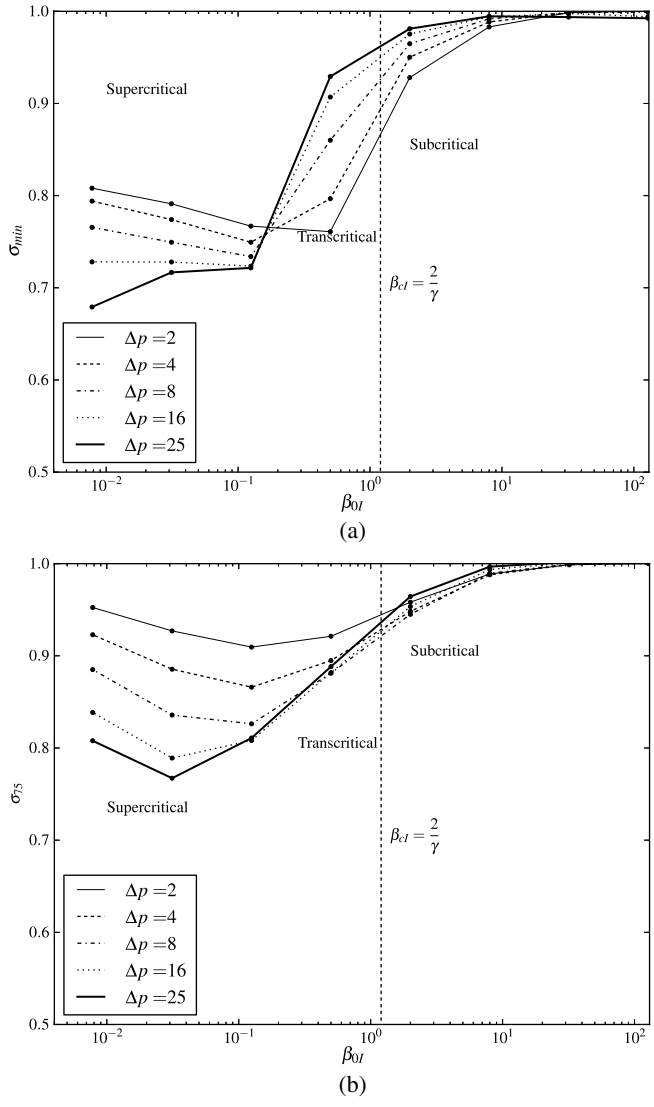

FIG. 15. Symmetry of the (a) primary (fast) shock system and (b) material interface for varying β_{0I} and Δp, measured at 75% the convergence time in case C3. Vertical dashed line indicates β_{cI}.

The subsequent increase in σ is due to the already-present kinks in the shocks at $\theta = 0$, which tends to accelerate those portions of the shock system faster than the non-kinked shocks. These kinks have an overcompensating effect, which in turn cause the symmetry parameter to rise above unity as the kinks approach the centre more quickly than the $\theta = \pi/2$ portions of the system. Note that we define major and minor axes according to *initial* shock speeds, not necessarily limiting the σ curve to an upper value of unity for all times.

Under the supercritical fields (for example, those in Figure 14), the fast shocks are initially very weak, as in the equivalent C1 fields; however, they strengthen as they converge. This is due to the natural acceleration of the converging shocks as well as the decreasing c_f toward the centre of the domain. As the magnetic field strength decreases, so do c_A and c_f; c_A approaches zero, and c_f approaches c for low θ; this has the effect of dramatically increasing the Mach number of the shock (with respect to c_f) as well as increasing the degree to which the shock can accelerate the flow before becoming intermediate, as the shocks move toward the centre. In fact, decreasing β_{0I} does not increase the (zero) magnetic field at the domain centre; it only increases the gradient of field variation away from the centre. Thus, the fast shock system will continue to strengthen no matter the initial interface β_I.

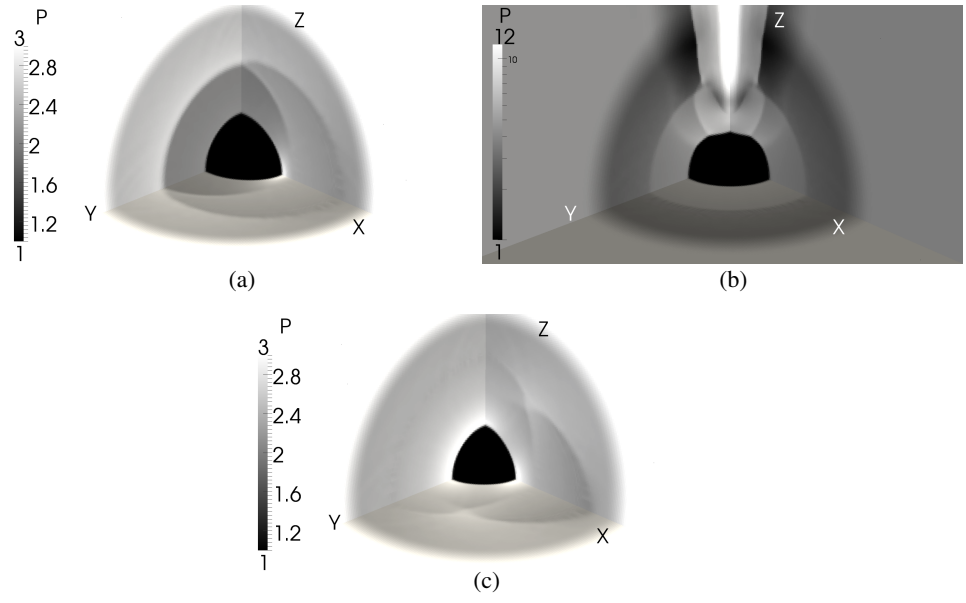

FIG. 16. Developed pressure fields on key planes, viewed in three dimensions, for all S-cases, $\beta_{0I} = 2$, $\Delta p = 2$. Case S2 (b) is shown on a logarithmic colour scale truncated at a peak of 12 for contrast. The true peak pressure in the high pressure region of (b) is $\simeq 33$. (a) Case S1, $t = 0.29$, (b) case S2, $t = 0.29$, and (c) case S3, $t = 0.34$.

Additionally, the fast shocks do not become as weak for supercritical fields as they do in C1. Evidence of these fast shocks are visible in Figure 14, which shows two strongly supercritical flows. By contrast, similarly supercritical flows in case 1 exhibit very weak fast shocks.

However, although the fast shocks in supercritical C3 do strengthen on convergence, and more so than in the C1 case, they are still quite weak, to the extent that we would otherwise not judge them to form the primary shock system; however, due to the complex interaction between the fast shocks and the field strength near the domain centre as described above, the flow becomes very complex after the fast shocks have converged and interfere with the slow shock system. In short, the convergence event of the fast shocks in C3 do have an effect on the rest of the flow structure in the long term; in contrast, the C1 fast shock system does not affect the rest of the flow in as complex a manner post convergence. For this reason, we examine the dynamics of the fast shock system in C3 rather than switching to the slow shock system in supercritical fields.

The compression caused by the fast shock system under supercritical fields remains strongly localized, and, before convergence, does not affect the slow shock geometry, which, as in case C1, still remains largely independent of β_{0I} and Δp for supercritical fields, as shown in Figure 14.

Figure 15 shows the symmetry of this fast shock system and the material interface for all β_{0I}, Δp. Subcritical flows generally see higher symmetry in case C3 than in C1—this is expected given the results shown in Figure 6 and discussed in Subsection IV A.

The regular shape of the slow shock structure in Figure 14 is due to a tendency of the shocks to straighten between kinks. These shocks do not remain straight for all times; at other times they may bend inwards or outwards.

Figure 15 also shows a clear switch in the role of Δp for strong supercritical fields; for these fields, increasing Δp shows a decrease in shock symmetry. This is because, for $\beta_I \gg \beta_{0I}$, the initial fast shocks near $\theta = 0$ are still necessarily weak—an increase in driving pressure does not promote an increase in shock speed, since $c_f \simeq c_I$ at these low θ angles; the $\theta = \pi/2$ shocks are more sensitive to this driving pressure and resolve more quickly into a diamond shape. An example of such a diamond shape can be seen in the fast shock systems in Figure 14. Further increasing the magnetic field slightly counteracts this effect. For all cases, however, the fast shock system strengthens as it converges, since the decreasing local magnetic field strength towards the centre allows a transition to subcritical fast shock behaviour.

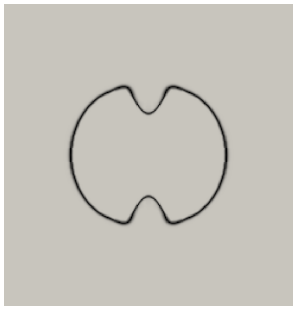

FIG. 17. Material interface position for case S2, $\beta_{0I} = 2$, $\Delta p = 2$, $t = 0.29$, in the x-normal plane. The depression at the poles is due to a high pressure jet impinging on the inner fluid.

Comparing Figures 15(b) and 11(b), there is similar behaviour in the contact surface across the parameter space. This is because of the contact surface being located in and around the slow shock system in both cases: since the slow shock system is subject to the same influences in both cases, its effect on the contact surface symmetry is also similar between cases, and hence the explanation for behaviour in Figure 15(b) is the same as in Subsection IV B 1.

C. Characterisation of 3D-spherical cases

In the spherical cases S1-3, the same flow features appear as in the cylindrical cases C1-3, and so the two geometries show fundamentally similar flows. The primary difference in the spherical geometry is an additional plane where the magnetic field topology is different to the other two orthogonal ones. In cases S1 and S2, the additional plane sees a magnetic field everywhere orthogonal to it; in case S3, the additional plane sees a magnetic field that apparently diverges from the origin. Case S3 also carries a magnetic field generated from current loops rather than current-arcs, and as such some symmetry is lost in the planes where the magnetic field is a saddle (see Sec. II). Figure 16 shows pressure fields for three key planes in each case, viewed in three dimensions. Cases S1 and S3 are axisymmetric around the x-axis, while case S2 is axisymmetric around the z-axis, similarly to the cylindrical geometry.

Figure 16 shows that, in the x-y plane, each case resembles its cylindrical counterpart. The greatest difference is seen in case S3, where the magnetic field is generated with current loops instead of current-carrying arcs, and the $\phi = \pm\pi/4$ symmetry planes have been lost; the kinks

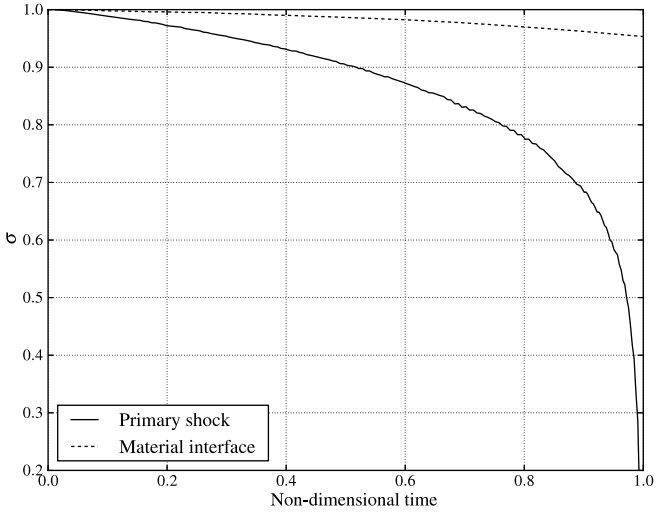

FIG. 18. Evolution of the symmetry parameter for the fast shock system and material interface in case S1, with $\beta_{0I} = 2$, $\Delta p = 2$, normalized to convergence time. The primary shock curve has been smoothed with a 3-point moving average.

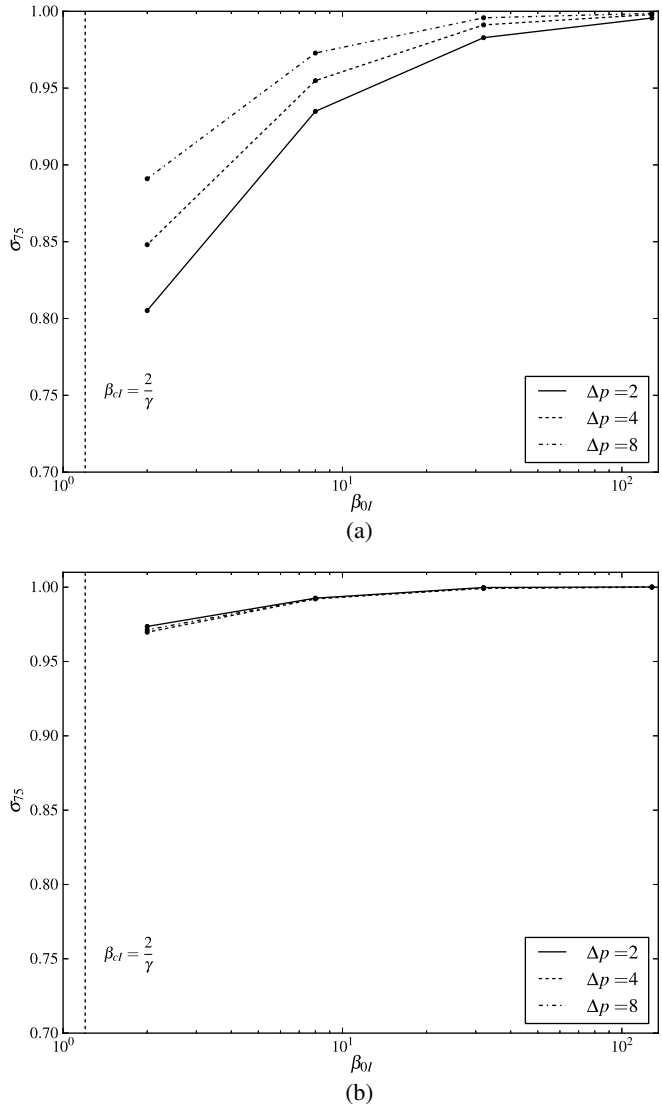

FIG. 19. Symmetry of the (a) primary shock system and (b) material interface for varying β_{0I} and Δp, measured at 75% convergence time in case S1. Black dashed lines indicate transcritical reference conditions.

appear at the same θ, however, and the general structure of the flow remains largely unchanged. The loss of the $\phi = \pm\pi/4$ symmetry planes does, however affect the σ evolution over time—this is examined in Subsection IV D 3.

In the x-normal plane, case S1 (Figure 16(a)) shows a uniform magnetic field that is everywhere tangent to the wave surfaces. The waves visible in this plane all coincide with the $\phi = \pi/2$ ray in the x-containing planes, and thus show an inward travelling fast shock, an outward-travelling fast expansion, and an inward-travelling TD.

In the same plane, case S3 (Figure 16(c)) shows a magnetic field that when projected onto the plane appears to diverge from the centre. Unlike case S1, the magnetic field angle in this plane is everywhere $\theta = 0$, and so the inward travelling jump is everywhere an HD shock, and the outward-travelling jump an HD expansion. As expected with $\theta = 0$, the CD is not visible in pressure. The high pressure visible behind the shock corresponds with the pressure at the kinks in the x-y plane.

In the z-parallel planes, such as x-normal, case S2 (Figure 16(b)) shows a dramatic influence of the current arcs attached to the Riemann interface's poles. These arcs form a Z-pinch—the Lorentz force ($(\nabla \times \mathbf{B}) \times \mathbf{B}$) term causes the plasma at these arcs to compress to very high pressures in a

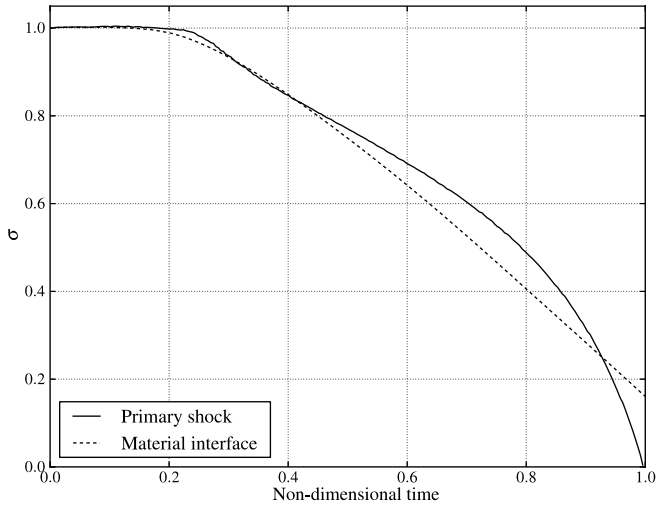

FIG. 20. Evolution of the symmetry parameter for the HD shock system and material interface in case S2, with $\beta_{0I} = 2$, $\Delta p = 2$, normalized to convergence time. Primary shock curve has been smoothed with a 3-point moving average.

short time. The high pressure from these Z-pinches then acts as jets, impinging on the inner fluid and forcing the HD shock system and material interface inwards, as seen in Figure 17. These jets also obscure what effect there may be of the discontinuity in the field's η-derivative at $\eta = r_w$ (see Sec. II B). The high-pressure jets furthermore have a clear effect on the symmetry of the case S2 problem, which we discuss further below.

D. Symmetry of 3D-spherical cases

The symmetry parameter σ in spherical geometry is still defined according to the ratio of minor and major axes as described in Sec. III and used in Subsection IV B; however, the additional dimension introduces an intermediate axis, that is, an axis along with a primary shock travels more quickly than along a major axis, and more slowly than along a minor axis. However, this intermediate axis is really only defined in case S3: in case S1, the x-normal plane is axisymmetric, and the fast shock system in that plane everywhere corresponds to the $\phi = \pm\pi/2$ shock in the z-normal plane; in case S2, the z-normal plane is axisymmetric, as in the cylindrical geometry. In case S3, however, the z-normal $\theta = 0$, $\theta = \pm\pi/4$, and $\theta = \pm\pi/2$ shocks all travel at different speeds (unlike in the cylindrical geometry, where the $\theta = 0$ and $\theta = \pi/2$ shocks were equivalent). Since it is not immediately clear whether the $\theta = 0$ or $\theta = \pi/2$ shock travels faster, all three axes—major, minor, and intermediate—exist within the z-normal plane. Except for this complication, discussed accordingly in Subsection IV D 3, the discussion proceeds as before.

1. Case S1

Figure 18 shows the spherical symmetry evolution for the fast shock system and the material interface in the reference case $\Delta p = 2$, $\beta_{0I} = 2$. The symmetry of both the fast shock system and the material interface behaves similarly to the cylindrical case, with just the convergence time decreased in the spherical geometry. Figure 19 shows the primary shock and contact surface symmetry across the parameter space. As with the cylindrical geometry, there is a decrease in the symmetry parameter with decreasing β_{0I}, while increasing Δp counteracts to some extent the field strength.

2. Case S2

The dramatic effect of the Z-pinch pressure jets on the symmetry of the shocks and interface in case S2 is clearly visible in Figure 20, which shows the reference case $\Delta p = 2$, $\beta_{0I} = 2$. This is the

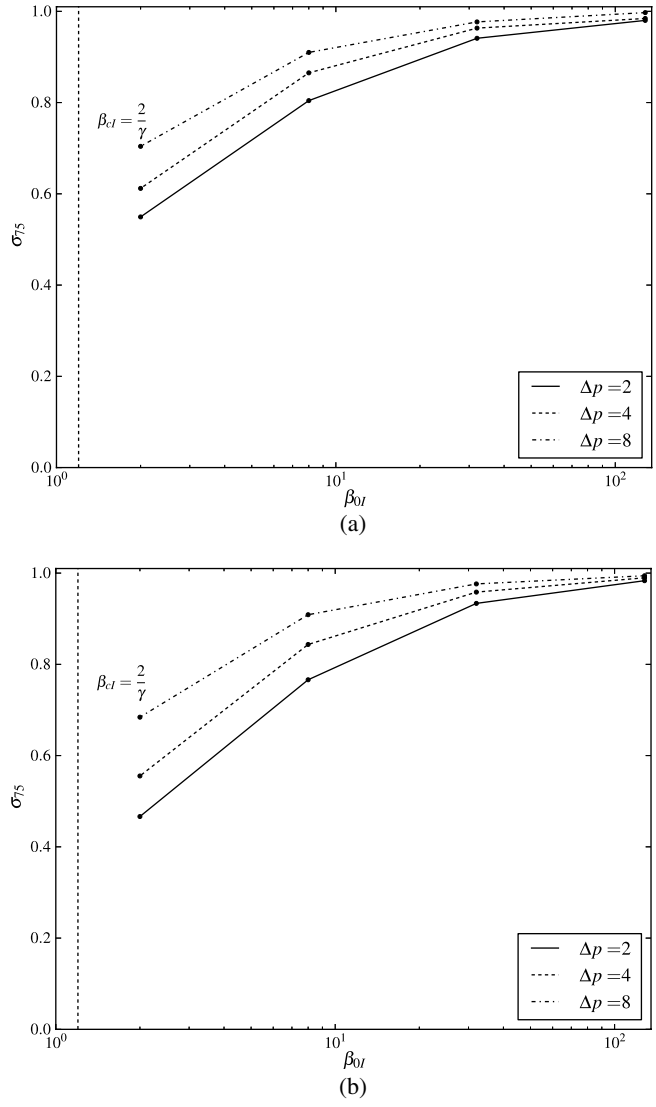

FIG. 21. Symmetry of the (a) primary shock system and (b) material interface for varying β_{0I} and Δp, measured at 75% convergence time in case S2. Black dashed lines indicate transcritical reference conditions.

only case that shows a strong decrease in the contact surface σ with time that is similar to the shock σ - this is due to the strong impingement from the high pressure jets at $\phi = \pm\pi/2$, while the $\phi = 0, \pi$ shock and contact surface remain unaffected.

As Figure 21 shows, the effect of the jet impingement on symmetry extends across most β_{0I} values; even $\beta_{0I} = 32$, which in other cases shows generally high σ_{75} values, is here reduced to around $\sigma_{75} = 0.9$ for $\Delta p = 2$. Increasing Δp serves to increase σ_{75}. This is because the Z-pinch forms due to the strong magnetic field near $\phi = \pm\pi/2$. The peak pressure in the jet also appears independent of Δp, so that any increase in Δp would increase the shock and contact surface velocity at $\phi = 0, \pi$ but not $\phi = \pm\pi/2$.

This disruption of symmetry makes a case S2 type field impractical in an ICF context, at least because of the presence of the high-pressure jets at the interface poles. We note also that this is the only case where the symmetry parameter of the material interface also drops below 0.9 for a subcritical field.

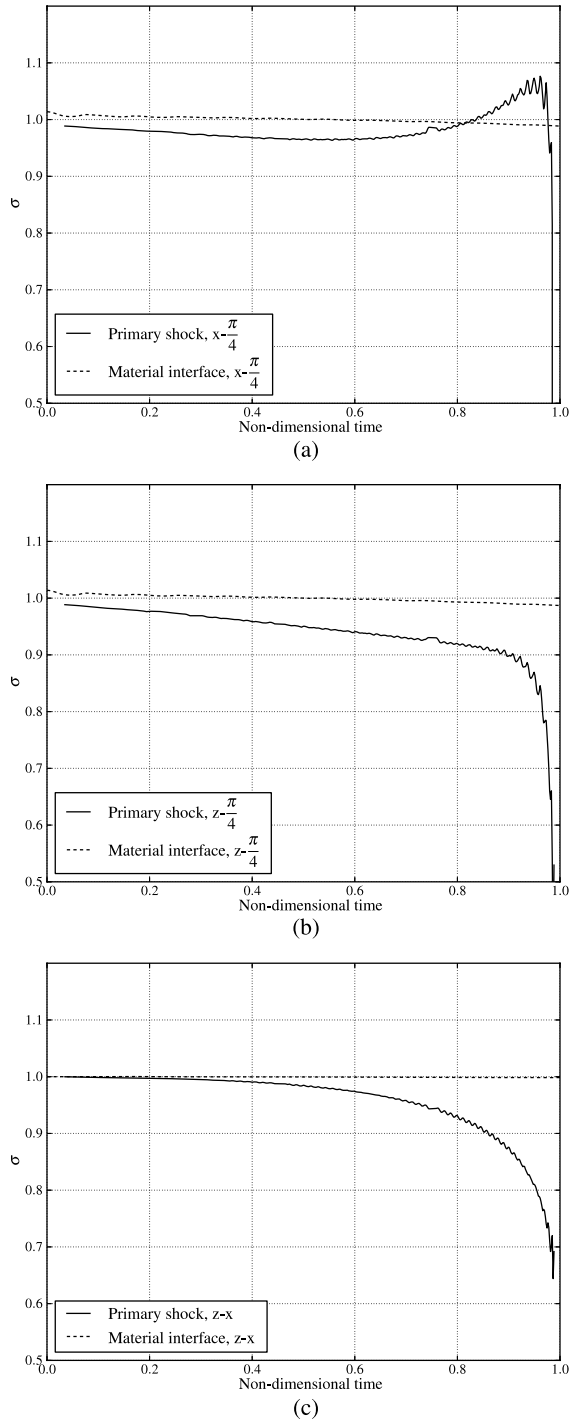

FIG. 22. Evolution of the symmetry parameter for the fast shock system and contact surface in case S3, with $\beta_{0I} = 2$, $\Delta p = 2$, normalized to convergence time; (a) shows σ treating the x-axis as the major axis and $\phi = \pi/4$ as minor; (b) treats the z-axis as major and $\phi = \pi/4$ as minor; and (c) treats the z-axis as major and the x-axis as minor. Primary shock curve has been smoothed with an 11-point average. (a) $x - \pi/4$ symmetry, (b) $z - \pi/4$ symmetry, and (c) $z - x$ symmetry.

3. Case S3

As mentioned in the introduction of Subsection IV D, there is an intermediate axis which influences the behaviour of σ. We identify this intermediate axis by examining the σ evolution curve for three arrangements of major-minor axes. Figure 22 shows this evolution of σ for each arrangement

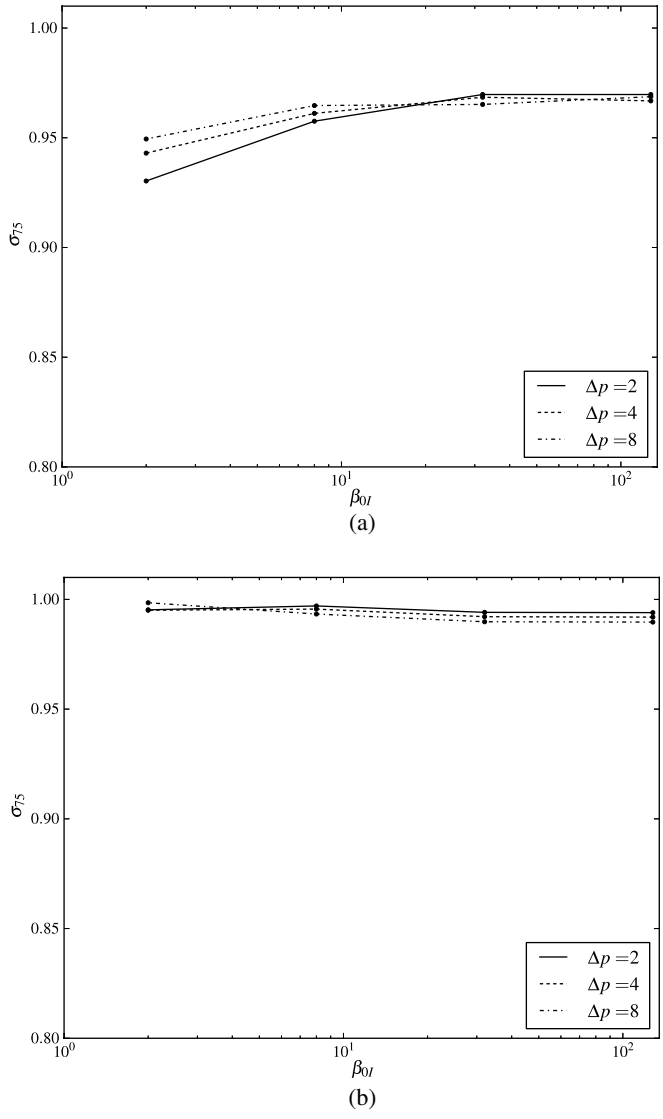

FIG. 23. Symmetry of the (a) primary shock system and (b) material interface for varying β_{0I} and Δp, measured at 75% convergence time in case S3. Black dashed lines indicate transcritical reference conditions.

under $\Delta p = 2$, $\beta_{0I} = 2$. In Figure 22(a), the major axis is taken along x and the minor axis along $\phi = \pm\pi/4$; in Figure 22(b), the major axis is taken along z (or any axis in the x-normal plane, which is axisymmetric); and in Figure 22(c), the major axis is taken along z and the minor along x. Although Figure 22(a) shows a similar graph to Figure 13, with the turning point due to the accelerating $\phi = 0$ shocks, Figures 22(b) and 22(c) both show graphs that lie below Figure 22(a); the σ_{75} is in fact lowest in Figure 22(b), on the $z - \pi/4$ arrangement, compared to the other arrangements. This implies that, for measuring σ_{75}, z is *the* major axis; $\phi = \pm\pi/4$ is *the* minor axis; and x is the intermediate axis for most of the implosion. This behaviour holds more strongly with increasing β in S3.

The turning point that is characteristic of the case C3 field is not present in the S3 $z - \pi/4$ arrangement seen in Figure 22(b). This is because the magnetic field is weaker around z than x, so that the increase of c_f away from $\theta = 0$ around $\phi = \pi/2$ is not as dramatic, and the local minimum in c_f at $\theta = \pi/2$ is not as pronounced as at $\theta = 0$, so that a kink that forms there is not as strong. The decrease in magnetic field as the shocks approach the centre still has an influence, so that the decrease in σ is not as pronounced as it is in spherical case 1 (compare Figure 18), but in any case, the kinks that form at the z-axis are not strong enough to cause a turning point in the σ graph.

Figure 23 shows that the behaviour described above is reflected across the parameter space. Varying β_{0I} and Δp otherwise has the same effect of subcritical fields as in case C3, showing a very symmetrical flow across all values. We conclude that the spherical form, S3, preserves the symmetry of the flow similarly to the cylindrical form, and in this respect remains a possibility for application to ICF.

V. CONCLUSION

The symmetry of three physically plausible magnetic field configurations (1, 2, and 3) was investigated under cylindrical (C) and spherical (S) converging Riemann problems in magnetohydrodynamics, with a view to understand the effect of a seed magnetic field on the dynamics of such implosions. The three configurations were a uniform, laterally applied seed field (C1, S1); a tangential field valued zero inside the Riemann interface (C2, S2) and a saddle-topology field (C3, S3). The investigation varied the field strength parameter β_{0I} and initial Riemann interface pressure difference Δp, and specifically examined the symmetry of the primary system, defined as the strongest shock system in terms of pressure ratio and the material interface.

Cases C1 and S1 showed a clear reduction in symmetry with increased magnetic field strength, with increasing Δp mitigating this effect. Case C2 was wholly axisymmetric, but S2 showed a strongly disrupted spherisymmetry in spherical geometry due to the formation of a Z-pinch at the poles of the Riemann interface. In cases C3 and S3, symmetry in both primary shocks and the material interface was strongly preserved for fields of $\beta_{0I} \geq 2$ and all Δp.

The primary shock system was identified as a fast shock system for most cases. For $\beta_{0I} \leq 1/2$ under cases C1 and C3, the slow shock system was the primary system due to a weakening of the fast shock system in terms of pressure ratio; however, in C3 the fast shock system, while not primary for these field strengths, was very interactive with the flow field. The C2 and S2 primary shock systems were hydrodynamic, since the field was zero inside the material interface in those cases, which acted as a magnetohydrodynamic tangential discontinuity.

In the context of cases C1,3 and S1,3, increasing Δp and β_{0I} both tend to drive the symmetry parameter towards unity for subcritical β_{0I}. A general increase in the parameter β_0, assuming subcritical β_{0I}, also suggested an increase in the spherisymmetry of the implosion. Out of the magnetic field configurations investigated, cases C3 and S3 appear most promising in terms of minimizing the asymmetry of implosion while applying a seed field to reduce heat losses and losses due to the Richtmyer-Meshkov and Rayleigh-Taylor instabilities.

ACKNOWLEDGMENTS

This research was supported under Australian Research Councils Discovery Projects funding scheme (Project No. DP120102378). W. Mostert is supported by an Australian Post-graduate Award. Dr Wheatley is the recipient of an Australian Research Council Discovery Early Career Researcher Award (Project No. DE120102942). Professor Samtaney is partially supported by a KAUST Base Research Award. We would also like to thank Myall Hingee for his useful contribution to the research.

APPENDIX: GENERATION OF SEED MAGNETIC FIELDS

The shape of the seed magnetic fields examined in this investigation was described in Sec. II B. They were constructed with the aim of physical plausibility to maintain relevance with ICF; a physical explanation of their formulation now follows. All variables are as defined in Section II.

Cases C1 and S1 see a unidirectional field of the form

$$\mathbf{B} = B_0 \hat{\mathbf{e}}_x \tag{A1}$$

a good approximation of which can be simply generated in reality, perhaps with a current loop at a suitable distance outside the domain, as seen in Chang *et al*. and related papers.[3,4]

Case C2 may be generated by considering a current running through the initial interface, in the z-direction. This gives a zero magnetic field inside the interface, and a purely tangential field outside the interface, hence, by Ampère's law

$$\mathbf{B}(r) = \begin{cases} (B_0 r_0/r)\hat{\mathbf{e}}_\phi & : r \geq r_0 \\ 0 & : r < r_0. \end{cases} \tag{A2}$$

The interface is, in C2, infinite in the z-direction. In S2, it is spherical and the field should be adjusted accordingly. Under spherical geometry, the tangential field is still generated by a current running through the interface; however, it now originates from one pole of the interface, at $x = y = 0$, $z = r_0$ and exits through the opposite pole at $x = y = 0$, $z = -r_0$. To allow the current to physically reach and exit the interface, two current arcs exist outside the interface on the z-axis. These current arcs have a set radius of r_w, which here are set to $r_w = r_0/15$.

This formulation allows the field in S2 to be purely tangential where it is non-zero. Outside the current arcs and interface, it follows Ampère's law. Inside the current arcs, the field varies linearly from the z-axis in the x–y plane. Note that on the x–y plane at $z = 0$, both C2 and S2 seed fields appear identical. As mentioned in Sec. II B, the field is discontinuous in its value at $r = r_0$ and in its η-derivative at $\eta = r_w$. Furthermore, for $\eta < r_w$, the curl of the field is non-zero, and in this sense the current is modelled.

The seed field in C3 may be generated by considering four infinite-length current arcs to run in the z-direction at (x_i, y_i) for the ith arc, which have current strength and direction given by the scaling parameter α_i, outside the computational domain. The resultant field is formed by superposition of Ampère's law for each current arc.

Though we might consider infinite current arcs in S3 as well, neglecting end effects, a more plausible field arises from sweeping the four current arcs into two current loops, located at x_i, for the ith loop, in the y–z plane. Generally, calculating the field from a current loop requires the use of elliptic integrals, with the result in the field components given by[26]

$$B_x = B_0 \frac{1}{\pi\sqrt{Q}} \left[E(k) \frac{1 - \varrho^2 - \chi^2}{Q - 4\varrho} + K(k) \right], \tag{A3}$$

$$B_r = B_0 \frac{\xi}{\pi\sqrt{Q}} \left[E(k) \frac{1 + \varrho^2 + \chi^2}{Q - 4\varrho} - K(k) \right]. \tag{A4}$$

To generate the field from two current loops, we centre the current loops at their positions $y = z = 0$, $x = x_i$ and superimpose their fields. This leads to Eqs. (14) and (15) given in Sec. II B. Note that C3 and S3 do not appear identical in the x–y plane at $z = 0$, unlike the other respective cases.

[1] R. L. Lindl and J. D. McCrory, "Progress toward ignition and burn propagation in inertial confinement fusion," Phys. Today **45**(9), 32 (1992).
[2] J. P. Knauer, O. V. Gotchev, P. Y. Chang, D. D. Meyerhofer, O. Polomarov, R. Betti, J. A. Frenje, C. K. Li, M. J.-E. Manuel, R. D. Petrasso, J. R. Rygg, and F. H. Séguin, "Compressing magnetic fields with high-energy lasers," Phys. Plasmas **17**, 056318 (2010).
[3] M. Hohenberger, P.-Y. Chang, G. Fiksel, J. P. Knauer, R. Betti, F. J. Marshall, D. D. Meyerhofer, F. H. Sguin, and R. D. Petrasso, "Inertial confinement fusion implosions with imposed magnetic field compression using the OMEGA laser," Phys. Plasmas **19**, 056306 (2012).
[4] P. Y. Chang, G. Fiksel, M. Hohenberger, J. P. Knauer, R. Betti, F. J. Marshall, D. D. Meyerhofer, F. H. Séguin, and R. D. Petrasso, "Fusion yield enhancement in magnetized laser-driven implosions," Phys. Rev. Lett. **107**, 035006 (2011).
[5] L. J. Perkins, B. G. Logan, G. B. Zimmerman, and C. J. Werner, "Two-dimensional simulations of thermonuclear burn in ignition-scale inertial confinement fusion targets under compressed axial magnetic fields," Phys. Plasmas **20**, 072708 (2013).
[6] W. Mostert, V. Wheatley, and R. Samtaney, "Characterisation of the cylindrical Riemann problem in magnetohydrodynamics," in *29th International Symposium on Shock Waves* (Springer, New York, 2013).
[7] A. B. Sefkow, S. A. Slutz, J. M. Koning, M. M. Marinak, K. J. Peterson, D. B. Sinars, and R. A. Vesey, "Design of magnetized liner inertial fusion experiments using the Z facility," Phys. Plasmas **21**, 072711 (2014).
[8] M. G. Haines, "A review of the dense Z-pinch," Plasma Phys. Controlled Fusion **53**, 093001 (2011).
[9] D. I. Pullin, W. Mostert, V. Wheatley, and R. Samtaney, "Converging cylindrical shocks in ideal magnetohydrodynamics," Phys. Fluids **26**, 097103 (2014).
[10] G. Whitham, "On the propagation of shock waves through regions of non-uniform area or flow," J. Fluid Mech. **4**, 337–360 (1958).

[11] T. J. Awe, R. D. McBride, C. A. Jennings, D. C. Lamppa, M. R. Martin, D. C. Rovang, S. A. Slutz, M. E. Cuneo, A. C. Owen, D. B. Sinars, K. Tomlinson, M. R. Gomez, S. B. Hansen, M. C. Herrmann, J. L. McKenney, C. Nakhleh, G. K. Robertson, G. A. Rochau, M. E. Savage, D. G. Schroen, and W. A. Stygar, "Observations of modified three-dimensional instability structure for imploding Z-pinch liners that are premagnetized with an axial field," Phys. Rev. Lett. **111**, 235005 (2013).
[12] R. D. Richtmyer, "Taylor instability in shock acceleration of compressible fluids," Commun. Pure Appl. Math. **13**, 297–319 (1960).
[13] J. D. Lindl, P. Amendt, R. L. Berger, S. G. Glendinning, S. H. Glenzer, S. W. Haan, R. L. Kauffman, O. L. Landen, and L. J. Suter, "The physics basis for ignition using indirect-drive targets on the National Ignition Facility," Phys. Plasmas **11**, 339–491 (2004).
[14] R. Samtaney, "Suppression of the Richtmyer-Meshkov instability in the presence of a magnetic field," Phys. Fluids **15**, L53–L56 (2003).
[15] V. Wheatley, R. Samtaney, and D. I. Pullin, "The Richtmyer-Meshkov instability in magnetohydrodynamics," Phys. Fluids **21**, 082102 (2009).
[16] V. Wheatley, D. I. Pullin, and R. Samtaney, "Stability of an impulsively accelerated density interface in magnetohydrodynamics," Phys. Rev. Lett. **95**, 125002 (2005).
[17] V. Wheatley, D. I. Pullin, and R. Samtaney, "Regular shock refraction at an oblique planar density interface in magnetohydrodynamics," J. Fluid Mech. **522**, 179–214 (2005).
[18] V. Wheatley, R. Samtaney, D. I. Pullin, and R. M. Gehre, "The transverse field Richtmyer-Meshkov instability in magnetohydrodynamics," Phys. Fluids **26**, 016102 (2014).
[19] J. Cao, Z. Wu, H. Ren, and D. Li, "Effects of shear flow and transverse magnetic field on Richtmyer-Meshkov instability," Phys. Plasmas **15**, 042102 (2008).
[20] V. Wheatley, R. Gehre, R. Samtaney, and D. I. Pullin, "The magnetohydrodynamic Richtmyer-Meshkov instability: The oblique field case," in *29th International Symposium on Shock Waves* (Springer, New York, 2013).
[21] Q. Zhang and M. J. Graham, "A numerical study of Richtmyer-Meshkov instability driven by cylindrical shocks," Phys. Fluids **10**, 974–992 (1998).
[22] S. H. R. Hosseini and K. Takayama, "Experimental study of Richtmyer-Meshkov instability induced by cylindrical shock waves," Phys. Fluids **17**, 084101 (2005).
[23] M. Lombardini and D. I. Pullin, "Small-amplitude perturbations in the three-dimensional cylindrical Richtmyer-Meshkov instability," Phys. Fluids **21**, 114103 (2009).
[24] K. O. Mikaelian, "Rayleigh-Taylor and Richtmyer-Meshkov instabilities and mixing in stratified cylindrical shells," Phys. Fluids **17**, 094105 (2005).
[25] J. Goedbloed, R. Keppens, and S. Poedts, *Advanced Magnetohydrodynamics* (Cambridge University Press, 2010).
[26] W. Smythe, *Static and Dynamic Electricity* (McGraw-Hill Book Company, 1950).
[27] R. Samtaney, P. Colella, T. J. Ligocki, D. F. Martin, and S. C. Jardin, "An adaptive mesh semi-implicit conservative unsplit method for resistive MHD," J. Phys.: Conf. Ser. **16**, 40 (2005).
[28] M. Berger and P. Colella, "Local adaptive mesh refinement for shock hydrodynamics," J. Comput. Phys. **82**, 64–84 (1989).
[29] P. Colella, D. Graves, T. Ligocki, D. Martin, D. Modiano, D. Serafini, and B. Van Straalen, "Chombo software package for AMR applications," in *Lawrence Berkeley National Laboratory Report* (Applied Numerical Algorithms Group, 2002).
[30] F. Stern, R. V. Wilson, H. W. Coleman, and E. G. Paterson, "Comprehensive approach to verification and validation of CFD simulations-Part 1: Methodology and procedures," J. Fluids Eng. **123**, 793 (2001).